



# Antimicrobial study and biosorption of Pb<sup>2+</sup> ions onto chitosan-walnut composites: mechanistic studies and neuro-fuzzy modeling approach

Abayomi Bamisaye<sup>1</sup> · Morenike O. Adesina<sup>1,2,3</sup> · Moses O. Alfred<sup>2,3</sup> · Mopelola Abidemi Idowu<sup>4</sup> · Oluwatobi Adeleke<sup>5</sup> · Kayode Adesina Adegoke<sup>6</sup>

Received: 4 November 2022 / Revised: 6 January 2023 / Accepted: 12 January 2023  
© The Author(s) 2023

## Abstract

The upsurge in the discharge of lead ions (Pb<sup>2+</sup>) into the environs resulting from various anthropogenic activities *vis-vis* its adverse effect on public health is a call for great concern. However, the adsorption technique, amongst other heavy metal removal methods, is regarded as the most promising. The present study synthesized a walnut shell-chitosan composite (WNS-CH) as an efficient biosorbent for Pb<sup>2+</sup> uptake and biofilter of *Bacillus subtilis* and *Klebsiella pneumoniae*. WNS-CH was characterized using SEM and FTIR. Furthermore, an intelligent and cost-effective machine learning model, an adaptive neuro-fuzzy model clustered with the grid-partitioning (GP), and fuzzy *c*-means (FCM) technique were developed to predict the adsorption of Pb<sup>2+</sup> based on relevant input parameters. The batch adsorption was carried out by varying operating parameters such as contact time, temperature, pH, adsorbent dose, and initial adsorbate concentration. The SEM images of WNS-CH showed a homogenous regular hollow ellipsoidal morphologies, while FTIR spectra showed the presence of O-H, N-H, C-N, and C-O. Under the conditions of initial pH 10, dosage 45 mg, and temperature of 40 °C, an adsorption efficiency of 94 % was obtained. The thermodynamic parameters,  $\Delta H^\circ$  and  $\Delta G^\circ$ , showed an endothermic and spontaneous process for Pb<sup>2+</sup> uptake. Antibacterial activities of the WNS-CH composite showed bioactivity against *Bacillus subtilis* and *Klebsiella pneumoniae* with a mean ZI of  $5.3 \pm 1.16$  and  $6.0 \pm 1.00$ , respectively. The experimental data was best described by Freundlich isotherm ( $R^2 = 0.9509$ ) and pseudo-first-order kinetic ( $R^2 = 0.9674$ ) models indicating chemisorption and multilayer adsorption process. The best prediction of Pb<sup>2+</sup> adsorption was obtained with the optimal GP-clustered ANFIS model using a triangular membership function (triMF), giving Root Mean Square Error (RMSE), Mean Absolute Deviation (MAD), Mean Absolute Percentage Error (MAPE), and correlation determination ( $R^1$ ) values of 1.217, 0.563, 1.698, and 0.9966 respectively at the testing phase. The GP-ANFIS model shows good agreement with experimental results. This study revealed that WNS-CH composite could be regarded as a promising biosorbent for the remediation of Pb<sup>2+</sup>-polluted wastewater. The cost analysis demonstrated that the WNS-CH composite could serve as an alternative to commercial activated carbon.

**Keywords** Biosorption · Chitosan-walnut shell · Antibacterial activity · Lead (II) ions · Adaptive neuro-fuzzy model

✉ Kayode Adesina Adegoke  
kwharyourday@gmail.com

<sup>1</sup> Department of Chemistry, Faculty of Natural and Applied Sciences, Lead City University, Ibadan, Oyo State, Nigeria

<sup>2</sup> African Centre of Excellence for Water and Environment Research (ACEWATER), Redeemer's University, PMB 230, Ede, Osun State, Nigeria

<sup>3</sup> Department of Chemical Sciences, Redeemer's University, PMB 230, Ede, Osun State, Nigeria

<sup>4</sup> Department of Chemistry, Faculty of Physical Science, Federal University of Agriculture, Abeokuta, Nigeria

<sup>5</sup> Department of Mechanical Engineering Science, University of Johannesburg, Johannesburg, South Africa

<sup>6</sup> Department of Chemical Sciences, University of Johannesburg, Johannesburg, South Africa

## 1 Introduction

Water is one of the essential components of the ecosystem in which the continuous existence of flora and fauna on planet earth is impinged on. Industrialization and other anthropogenic activities have threatened the aqueous environment, thus endangering the hydrosphere due to the introduction of contaminants and toxic materials [1] which can be categorized as chemical and biological contaminants. The chemical pollutant sources include contamination due to domestic wastes (sewage and sludge), industrial waste such as insecticides and herbicides producing industries, food processing waste, mining industries, pharmaceutical industries, textile industries, pollutants from livestock operations, metal plating facilities, refineries, and polymer industries [2].

Research has shown that the major contaminant associated with all these anthropogenic activities is the introduction of heavy metals. The bioavailability and toxicity of these metals depend on the state or the environmental condition. Synergistic effects of  $Pb^{2+}$  in the aquatic environment have been shown to cause structural damage or physiological alteration in the fin, alteration of hepatocytes in fishes, and some other aquatic fauna [3, 4]. Due to their non-biodegradable nature, they tend to be persistent in the environment and could be bioaccumulated in aquatic plants and animals [2], which could find its way into the human food chain. Moreover, aquatic fauna served as one of the major sources of protein to humans. They are said to be lethargic even at a low concentration of 10  $\mu\text{g}/\text{dL}$  for adult and for children 5  $\mu\text{g}/\text{dL}$ , resulting in a series of chronic health challenges in humans [2, 5]. Some of such lethargic impact includes live or kidney damages, abnormality of endocrine glands and cardiovascular, gastrointestinal, and central nervous system [6–8]. Also, viruses, bacteria, and other microbes in water have been shown to cause cholera, dysentery, typhoid fever, etc. These are common waterborne diseases [9]. This type of contamination is also majorly attributed to human and animal waste due to the discharge of pathogenic microorganisms into water bodies [10, 11].

Several methods have been in place to rid the water body of these toxicants to achieve a contaminant-free aquatic environment. These techniques include reverse osmosis, ultrafiltration, ion-exchange, chemical precipitation, phytoremediation, and adsorption [11, 12]. However, adsorption has gained wide interest because of its advantages such as versatility and ease of operation, among others [12, 13]. The commonly used adsorbent for water purification is activated carbon (AC), but it suffers a setback due to high cost of production. Therefore, efforts have focused on the facile preparation of cheap, easy to

prepare, versatile, and efficient adsorbent, which can easily be prepared and utilized in rural settings to remove water contaminants. This necessitated the development of cost-effective alternative technologies, thereby resulting in the emergence of agricultural waste *vis-à-vis* its composite as an alternative for the development of economical and eco-friendly treatment process of wastewater.

Biosorption is a technique that involves selective sequestration of contaminants in water by using plant or animal-based adsorbent [14, 15]. This has been reportedly employed for the decontamination of industrial effluents. An efficient adsorption process of removing heavy metals present in simulated or real wastewater using low-cost plant-based adsorbents has been demonstrated [15–18], for instance, biosorption of lead ions from its solution using biomass and biomass-based adsorbents [14, 19, 20]. Various studies on the biosorption of various toxic metals, namely,  $Pb^{2+}$ , Zn, and  $Cd^{+}$ , have been reported [11, 21]. Other biosorption studies have employed Mango peel [22], orange peel [23], *Theobroma cacao* pod [4], and banana peel [24].

Furthermore, the excellent ecofriendly characteristics of chitosan which includes biodegradability, nontoxicity, biocompatibility, good antimicrobial properties, and ability to chelate with a series of chemical substances have accorded it a great attention for potential application in wastewater treatment. This scavenging potential is due to the presence of amino ( $-\text{NH}_2$ ) and hydroxyl ( $-\text{OH}$ ) moiety in chitosan molecule [25]. However, research has shown that the active sites which are responsible for adsorption purposes could not be directly accessed by potential adsorbents [26]. This is as a result of the conformation and configuration of linear chains of chitosan which crystallizes with another chain through the formation of hydrogen bond thus resulting to the poor solubility and reactivity of chitosan. In order to address these challenges and thus harness the adsorptive potential of chitosan, it is therefore imperative to modify it with a low cost and environmentally friendly material thus forming a composite.

Recently, composites have been synthesized for heavy metal adsorption from an aqueous solution. Unuabonah et al. [27] developed a composite constituting *Carica papaya* seeds and *Musa paradisiaca* (plantain peels), which demonstrated better affinity for phosphate ions while chitosan-functionalized eggshell for the removal of  $\text{Cu}^{2+}$  ion from aqueous solution [28] has also been reported. However, there is no report on the antimicrobial study of chitosan/walnut composites and their mechanistic biosorption behavior for  $Pb^{2+}$  ions from wastewater.

For the first time, the present study describes the development of chitosan biomass-based composite materials for the antimicrobial activity and efficient adsorptive removal of  $Pb^{2+}$  ions from an aqueous solution. The study was carried out to harness the viability of walnut shell—an agricultural

waste—as potential adsorbent to ameliorate the challenges associated with agricultural waste management and heavy metal pollution control. Furthermore, this study is aimed at enhancing the uptake capacity of these biomass materials by functionalizing with chitosan for better and maximum removal of  $\text{Pb}^{2+}$  ions. The procedures for synthesizing the aforementioned materials for this study are not cumbersome and thus amenable for industrial scale-up and eco-friendly fabrication.

## 2 Materials and methods

### 2.1 Preparation of the adsorbents

The walnut fruits were obtained from Kuto market, Abeokuta, Ogun state, Nigeria. The shells were crushed and were thoroughly washed with distilled water in order to remove the dirt. The walnut shells (WNS) were air-dried, ground to powder using an electrical blender. The resultant was sieved using British Standard Sieves with 100  $\mu\text{m}$  mesh size in order to obtain a fine particle. Chitosan (CH) was obtained from Sigma Aldrich. The WNS–CH composites were obtained by dissolution of CH and WNS separately in 2 and 10 % aqueous acetic acid, respectively. Furthermore, WNS was treated with 2 %  $\text{NaHCO}_3$  for neutralization. Then, the neutralized WNS solution was added to CH solution, and the mixture was treated with an alkaline coagulant solution at ratio of 5:4:1 *w/w* of  $\text{H}_2\text{O}$ , MeOH and NaOH, respectively. The WNS–CH (5:1) composite thus obtained was washed with distilled water, oven dried at 60 °C for 10 h, and stored for further experimental use.

### 2.2 Adsorbate

Analytical grade chemicals were used in this study without further purifications. The standard solution of Pb (II) was prepared from  $\text{Pb}(\text{NO}_3)_2$  by dissolving 1.598 g of the salt in 1,000 mL distilled water. This stock solution was then diluted to required concentrations, and the pH values of resulting solutions were adjusted using a digital pH meter to desired values with 1.0 mol/L NaOH or HCl. Different concentrations were prepared from the respective stock solution using serial dilution.

### 2.3 Characterization of the biosorbent

Determination of the morphological changes in the adsorbent before modification with CH, after modification and adsorption of metal ion, was observed using a scanning electron microscope (SEM) (Tescan, UK). The surface chemistry of the adsorbents was analyzed with the Fourier transform infrared spectroscopy (FT-IR) (Buck Scientific, Model 530M, USA)

with KBr disk technique used to establish the main functional groups present on the adsorbent and their interaction with the metal ions.

### 2.4 Adsorption equilibrium study

The batch adsorption experiments were carried out by exposing 50 mL of 20 mg/L  $\text{Pb}^{2+}$  solution to 300 mg of WNS-CH composite in 250 mL Erlenmeyer flasks. These were allowed to reach equilibrium in an orbital shaker (Thermo Fisher scientific, USA) at 180 rpm for 120 min after which the aliquots were withdrawn and filtered. The filtrate was analyzed for residual  $\text{Pb}^{2+}$  concentration using an AAS spectrophotometer (Buck Scientific, 200 series, USA). The quantity of the pollutants adsorbed onto unit weight of the adsorbents was calculated using Eqs. (1) and (2)

$$q_e = \frac{(C_o - C_e)V}{m} \quad (1)$$

$$\%R = \frac{C_o - C_e}{C_o} \times 100 \quad (2)$$

where  $q_e$ ,  $C_o$ , and  $C_e$ ,  $V$ ,  $m$ , and  $\%R$  represent the amount of pollutant adsorbed (mg/g), initial and equilibrium liquid-phase concentrations of the pollutants (mg/L), the volume of the solution (L), weight of the sorbent used (g), and percent pollutant removal respectively. The data obtained were fitted to the adsorption and kinetic models for a better understanding of adsorption process.

### 2.5 Isotherm models

In order to optimize the design of an adsorption system for the removal of adsorbate ( $\text{Pb}^{2+}$ ), different models were used to explain the relation between adsorbate equilibrium concentration on the solid phase and in the liquid phase at room temperature. This is useful in establishing the most suitable correlation for the adsorption equilibrium curves. In this study, the nonlinear expression of Langmuir (Eq. 3), Freundlich (Eq. 4), Langmuir-Freundlich (Eq. 5), Brouers Sotolongo (Eq. 6), and Temkin (Eq. 7) were applied. The nonlinear equations representing these isotherm models are illustrated below:

$$q_e = \frac{Q_m K_L C_e}{1 + K_L C_e} \quad (3)$$

$$q_e = K_F (C_e)^{1/n} \quad (4)$$

$$q_e = \frac{Q_m (k_a C_e)}{K_a C_e + 1} \quad (5)$$

$$q_e = q_m \left( 1 - \left( e^{(k_w | C_e)^\alpha} \right) \right) \quad (6)$$

$$q_e = q_m \ln (K_T C_e) \quad (7)$$

where  $q_e$  is amount of pollutant adsorbed at equilibrium,  $q_{max}$  is maximum adsorption capacity (mg/g),  $C_e$  is the equilibrium concentration (mg/L),  $K_F$  is Freundlich constant,  $n$  equals to adsorption intensity,  $Ka$  is affinity constant for adsorption (L/mg),  $K_w$  is index of heterogeneity  $K_F/q_{max}$ , and  $\alpha$  measures the energy heterogeneity of the adsorbent of the adsorbent surface [29].

## 2.6 Effects of process variables

The effect of initial metal ion concentration ranging from 20 to 100mg/L on the adsorption of  $Pb^{2+}$  using 300mg WNS-CH composite was studied. For the effect of adsorbent dose, the dose was varied from 150 to 450 mg, while the effect of pH was studied using initial solution pH values ranging from 2.0 to 10.0. The solution pH was adjusted with 0.1M HCl and 0.1M NaOH. And finally the effect of solution temperature was examined between 10 and 50 °C on adsorption of 20 mg/L  $Pb^{2+}$  Kinetic 4studies. This gives important details on the reaction pathway and provides a better explanation of the relationship between amounts of pollutant removal and the rate of adsorption. For the sake of this study, a similar experiment in the adsorption equilibrium study was carried out; however, aliquots were withdrawn from the reaction medium at intervals of 5, 10, 20, 40, 60, 80, 100, 120, 140, and 160 min and analyzed for the concentration of residual  $Pb^{2+}$  in solution. The experimental data were fitted to the pseudo-first-order (PFOM), pseudo-second-order (PSOM), and the Brouers-Sotolongo Kinetic models (BS). By applying these models, the correlation coefficient,  $R^2$ , can be determined.

The general expression for the pseudo-first-order kinetic models is

$$\frac{dq_t}{dt} = k_1 (q_e - q_t) \quad (8)$$

where  $k_1$ ,  $q_e$ ,  $q_t$  represent rate constant of the PFOM sorption ( $\text{min}^{-1}$ ), the amount of adsorbed adsorbate at equilibrium (mg/g), and the amount of adsorbate adsorbed at time  $t$  (min) (mg/g), respectively.

The nonlinear expression for the PFOM is

$$q_t = q_e - q_e e^{-k_1 t} \quad (9)$$

The PSOM equation is given as [30]

$$\frac{dq_t}{dt} = k_2 (q_e - q_t)^2 \quad (10)$$

While the nonlinear form is given as

$$q_t = \frac{k_2 q_e^2 t}{(1 + q_e k_2 t)} \quad (11)$$

The BS interpolates between the PFOM and PSOM kinetics, and it introduces  $n$ ,  $a$  (a fractional order), which characterizes the time variation of  $k_2$ . The equation for the BWS is given as

$$q_{n,a}(t) = qe \left[ 1 - \left[ 1 + [n - 1] \left[ t / \tau_{n33,a} \right]^\alpha \right]^{-1/(n-1)} \right] \quad (12)$$

Also, the experimental data for the effect of temperature was fitted into the Vant Hoff equation to obtain the thermodynamic parameters:

$$\ln K_C = \frac{\Delta S^\circ}{R} - \frac{\Delta H^\circ}{RT} \quad (13)$$

where  $\Delta S^\circ$  is entropy change ( $\text{J}\cdot\text{mol}^{-1}\cdot\text{K}^{-1}$ ),  $\Delta H^\circ$  is enthalpy change ( $\text{J}\cdot\text{mol}^{-1}$ ),  $R$  is universal gas constant ( $8.314 \text{ J}\cdot\text{mol}^{-1}\cdot\text{K}^{-1}$ ),  $T$  is absolute temperature (K), and  $K_C$  is the dimensionless thermodynamic equilibrium constant calculated using the Eq. 14 [31].

$$K_C = M_w \times 55.5 \times 1000 \times qe \quad (14)$$

where  $M_w$  is the atomic weight of the  $Pb^{2+}$  ( $207.4 \text{ g}\cdot\text{mol}^{-1}$ ), the factor 55.5 is the number of moles of pure water per liter (1000 g/L divided by 18 g/mol), and  $qe$  (mg/g) is the adsorption equilibrium constant for the adsorption of  $Pb^{2+}$  at different temperature (10–50 °C) onto WNS-CH.

$$\Delta G(\text{ Gibbs free energy (J/mol)}) = \Delta H - T\Delta S \quad (15)$$

## 2.7 Experimental procedure for the antimicrobial study of WNS-CH composite

### 2.7.1 Preparation of inoculums

For inoculum's preparation, Mueller Hinton broth was prepared according to the manufacturer's instruction and 5 mL of broth medium was dispensed into each screw capped test tube and sterilized by autoclaving at 121°C for 15 min. The test tubes were cooled and kept in an incubator for 24 h at 37 °C to check sterility. The isolates were inoculated into the sterilized test tubes containing the medium and placed in an incubator overnight at 37 °C.

The presence of turbidity in broth culture was adjusted equivalent to 0.5 McFarland standards to obtain standardized suspension by adding sterile normal saline or broth to obtain a turbidity optically comparable to that of the 0.5 McFarland standard or against a white background with contrasting black line. The McFarland 0.5 standard provides turbidity comparable to bacterial suspension containing  $1.5 \times 10^8$  CFU/mL [32]

Note this was used (suspension) within 5 min to avoid population increased.

### 2.7.2 Determination of antimicrobial activity (agar well diffusion method)

Antibacterial activities of the biosorbent on *Bacillus subtilis* and *Klebsiella pneumoniae* were evaluated by the well plate agar diffusion method using the modified Aida *et al.* method [33]. The bacterial cultures were adjusted to equal 0.5 McFarland turbidity standards and inoculated on nutrient agar plate (diameter 9 cm) by flooding the plate with 1 mL of each of the standardized test organism; swirled and excess inoculum was carefully decanted. A sterile cork borer was used to make wells (6 mm in diameter) on the agar plates.

The composite was dissolved in dimethyl sulfoxide (DMSO). DMSO was taken as negative control, and a different concentration of WNS-CH composite solutions was prepared. These solutions were applied on each of the well in the culture plates previously inoculated with the test organisms and left on the bench for 1 h for proper diffusion of the samples with a micropipette. Thereafter, the plates were incubated at 37 °C for 24 h. Antibacterial activity was determined by measuring the zone of inhibition around each well.

### 2.8 Adaptive neuro-fuzzy inference system

Adaptive neuro-fuzzy inference system (ANFIS) combines the learning ability of artificial neural network (ANN) and fuzzy inference systems (FIS) adaptively with the antecedent and consequence elements connected by fuzzy rules [29, 34]. ANFIS contains a set of fuzzy IF-THEN rules that have the learning ability to approximate nonlinear functions. It is a multilayer, adaptive, and feedforward network that estimates precise and uninterrupted functions. The model uses the least-square method, hybrid learning algorithm, and the

backpropagation gradient-descent methods that enhance the resulting linear parameters of the output and the nonlinear premises parameter with fuzzy membership [35, 36]. Eqs. 16 and 17 represent the set of fuzzy inference rules for two inputs  $x$  and  $y$  and an output  $F$ .

$$\text{Rule 1 : If } x \text{ is } A_1 \text{ and } y \text{ is } B_1, F_1 = p_1x + q_1y + r_1 \quad (16)$$

$$\text{Rule 2 : If } x \text{ is } A_2 \text{ and } y \text{ is } B_2, F_2 = p_2x + q_2y + r_2 \quad (17)$$

where  $A_1, B_1, A_2, B_2$  are membership functions,  $x$  and  $y$  are input parameter, and  $F_1$  and  $F_2$  are outputs acquired from the system, while  $p, q,$  and  $r$  are nodal consequent parameters. Figure 1 represents the architectural framework of the ANFIS with five layers.

At the first layer called the fuzzy layer, the membership grade at each node  $j$  is generated and contains the input and output functions as expressed in Eq. 18. The output function is defined by  $F_{1j}$ , while  $\tau A_i(x)$  and  $\tau B_i(y)$  define the membership functions.

$$F_{1j} = \tau A_i(x) \text{ and } F_{1j} = \tau B_i(y) \quad (18)$$

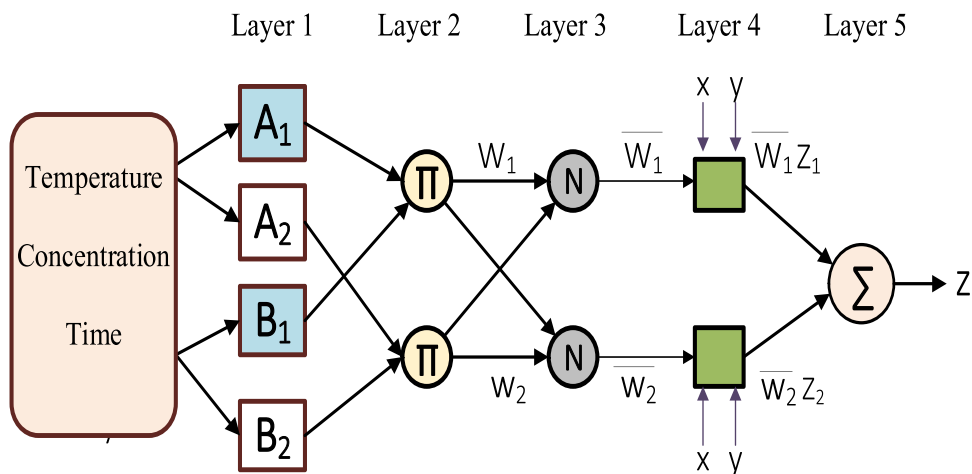
The second layer is the product layer where all the nodes are fixed while the output represents the firing strength ( $w_1$ ) estimated through multiplication in each nodes. The fuzzy layer's output becomes the product of the signal for the input as expressed in Eq. 16.

$$F_{2j} = \tau A_i(x) \times \tau B_i(y) \quad (19)$$

At the normalization layer, output is a fraction of the firing strength of the node to the sum of all firing strength of the other nodes as in Eq. 20.

$$F_{3j} = \bar{w}_i = \frac{w_1}{w_1 + w_2 + w_3}, \quad (20)$$

Fig. 1 Architectural framework of the ANFIS structure



At the defuzzification layer, the signal from the normalization layer is multiplied with fuzzy rule's function such that the output  $F_{3j}$  is expressed as given in Eq. 21.

$$F_{4j} = \bar{w}_j f_i = w_1 (p_1 x + q_1 y + r_1) \quad (21)$$

At the fifth layer, the output is computed. In this layer, a single node calculates the total output by adding all signal from all layers using a summation function as given in Eq. 22.

$$F_{5j} = \sum_{i=1}^n \bar{w}_j f_i = \frac{\sum_{i=1}^n w_i f_i}{\sum_{i=1}^n w_i} \quad (22)$$

## 2.9 Data clustering

In neuro-fuzzy-based modeling, clustering is a critical requirement for grouping data points into a similar fuzzy cluster, assigning membership functions (MF) and generating fuzzy inference system (FIS) structure for the data. It has been used to describe the connections between unlabeled data sets, thereby establishing a high degree of intersimilarity within and across clusters [37, 38]. This technique entails classification of a data set  $C$  into cluster sets  $Q_i$  ( $\subseteq i = 1, 2, 3, \dots, q$ ) in an unsupervised approach, i.e., without a preknowledge of the information about the data structure such as the group numbers, cluster members, and their definition. This is achieved with common clustering algorithms, namely, grid partitioning, subtractive clustering, and fuzzy  $c$ -means. There is a careful selection of clustering techniques in ANFIS modeling owing to its significant effects on the performance of the model in approximating an output function. The fuzzy  $c$ -means and the grid-partitioning method are selected to optimal design the best model for the prediction of the removal rate in this study. The significant difference in the intensity and computation speed and time of these two techniques as a basis for comparing their performances has motivated their choice.

### 2.9.1 Fuzzy $c$ -means clustering

Fuzzy  $c$ -means (FCM) is a data clustering technique that groups a data set into clusters such that each data point belongs to every cluster to a certain degree. This technique clusters a finite set of data  $X = (x_1, x_2, \dots, x_m)$  into cluster numbers in an iterative minimization steps, where  $x_i$ ,  $i = 1, \dots, m$  is a  $l$ -dimensional vectors [39]. The fuzzy  $c$ -means clustering is preferred for an application where speed is preferred due to its speed boost capacity, thus motivating its choice in this study [36]. The objective function of the FCM clustering which minimizes the distance center is given in Eq. 23 [40].

$$\min_{U,V} C(U, V) = \sum_{i=1}^n \sum_{j=1}^c U_{ij}^m d_{ij}^2 \quad (23)$$

$$0 \leq U_{ij} \leq 1, \quad \sum_{i=1}^c U_{ij} = 1, \quad 0 < \sum_{i=1}^n U_{ij} < n \quad (24)$$

The local minimum of  $J_{FCM}$  can be reached by meeting up with the following conditions:

$$U_{ij} = \frac{1}{\sum_{k=1}^c \left( \frac{d_{ij}}{d_{ik}} \right)^{\frac{2}{m-1}}} \quad (25)$$

and

$$V_j = \frac{\sum_{i=1}^n U_{ij}^n x_i}{\sum_{i=1}^n U_{ij}^m} \quad (26)$$

### 2.9.2 Grid partitioning

This is a clustering technique in which the input space is divided into rectangular subspace through the use of a few local fuzzy regions by axis-parallel partition depending on the type and number of the pre-defined membership function [41]. In the exponential relationship between the number of fuzzy rules  $m$  and the number of input  $m$  resulting number of fuzzy rules in the order  $n^m$ , thus, a small number of membership function requirement has been necessitated. This demerit of this technique is a major setback because it consequently results in a large memory prerequisite and often led to curse dimensionality [34] which indicates that the number of samples needed to estimate an arbitrary function with a given level of accuracy grows exponentially with respect to the number of input variables (i.e., dimensionality) of the function. It means that the number of objects in the data set that need to be accessed grows exponentially with the underlying dimensionality. This exponential growth leads to a more computationally intense model due to the higher memory size and time required. Abonyi et al. describe the grid partitioning clustering technique in details [42].

## 2.10 Building the neuro-fuzzy model

An optimal model building of the neuro-fuzzy model was carried out in this study to predict the residual rate by checking the impact of the hyperparameters of the clustering algorithm on the model's performance. The significant difference in the intensity and computation speed and time of these two techniques as a basis for comparing their performances has motivated their choice. The FCM and GP techniques were used in this study to generate the fuzzy inference system. A range of 2–8 number of clusters was optimized for the FCM algorithm

to optimally select the best model which gives the best performance. The prominent input membership types are gaussMF, triMF, trapMF, and gauss2MF while a linear output membership function type was tested for the GP technique. Other parameters specified for the model are presented in Table 1. The training was done using the 70 % of the experimental data set while the remaining 30 % hold-out data were used for testing the model’s accuracy. Before building the model, the data used for training was normalized with Eq. 27 to ascertain that they were in the same range.

$$y_{norm} = \frac{x - x_{min}}{x_{max} - x_{min}} \tag{27}$$

where  $y_{norm}$  = the normalized data,  $x$  = the mean of the variable,  $x_{min}$  = minimum variable, and  $x_{max}$  = maximum variable. The scripts for the algorithm were computed on MATLAB (R2015a) installed on a computing device with 64 bits, 4GB ram Intel(R) core(TM)i3 configuration. The parameters specified for the algorithm are presented in the model presented in Table 1.

Model performance and the fitness between the data were evaluated using statistical metrics, namely, Mean Absolute Percentage Error (MAPE), Mean Absolute Deviation (MAD), Root Mean Square Error (RMSE), and correlation coefficient ( $R^2$ ). They are computed as presented in Eqs. 28–31 respectively.

$$MAPE = \frac{1}{N} \sum_{i=1}^N \left| \frac{O_i - P_i}{O_i} \right| \times 100\% \tag{28}$$

$$MAD = \sum_{i=1}^N \frac{(O_i - P_i)}{N} \tag{29}$$

$$RMSE = \left( \sum_{i=1}^N \frac{(P_i - O_i)^2}{N} \right)^{1/2} \tag{30}$$

$$R^2 = 1 - \left[ \frac{\sum_{i=1}^n (O_i - O)(P_i - P)}{\sqrt{\sum_{i=1}^n (O_i - O)^2 \times \sum_{i=1}^n (P_i - P)^2}} \right]^2 \tag{31}$$

where  $N$  = the number of samples,  $i$  = the sample index,  $P_i$  = value of the predicted outcome for  $i$ th sample,  $O_i$  = experimental outcome for the  $i$ th sample,  $O$  = average experimental outcome, and  $P$  = average predicted outcome.

### 3 Results and discussion

#### 3.1 Antimicrobial study of WNS-CH composite

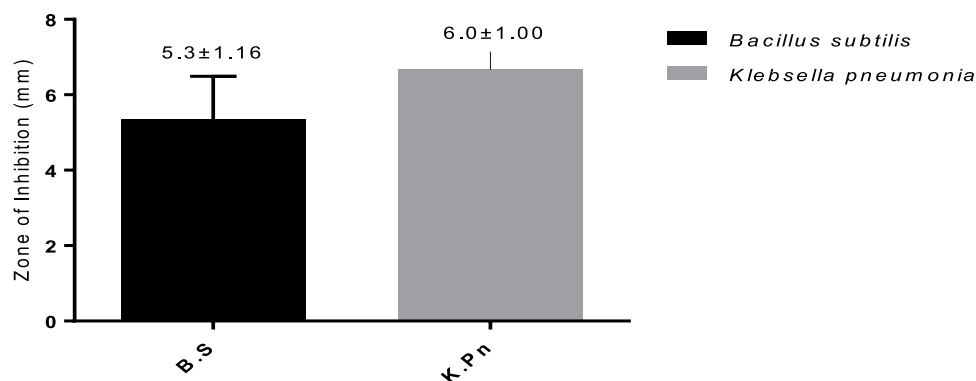
The antibacterial behavior of WNS-CH composite against *Bacillus subtilis* and *Klebsiella pneumonia* was examined by measuring the observed zones of inhibition, thereby showing the antibacterial activity of WNS-CH as presented in Fig. 2. These microorganisms have been noted to be one of the major causes of wound infections and food contamination. The synthesized composites recorded outstanding bioactivities against the test organisms. A recorded mean ZI of  $5.3 \pm 1.16$  mm was noted on *Bacillus subtilis*, while  $6.0 \pm 1.00$  mm was recorded on *Klebsiella pneumoniae*. The biological activity of the synthesized composite could be attributed to the interaction between the adsorbent and the lipid-bilayer cell membrane of the microorganisms [43]. Due to the interionic interaction between the charged surface of the bacterial cell membrane and the functional groups (such as  $-NH$ ,  $-COOH$ , and  $-SH$ ) of the composite thereby leading to the disruption of the microorganism cytomembrane/cell.

The complexation due to functionalization of WNS with CH molecule improves the lipophilicity of the adsorbent surface thereby facilitating the WNS-CH composite-lipid bilayer interaction of the microorganism and as such increased intracellular rapid uptake and permeation of the composite through the cell membranes of *Bacillus subtilis* and *Klebsiella pneumonia* [44]. The antimicrobial activity

**Table 1** Specified control parameters for the FCM and GP clustered-ANFIS model

Clustering	Parameters	Values/range of values
FCM	FIS structure	Takagi-Sugeno-type
	Number of clusters	2–8
	Number of exponent for matrix portioning	2
	Maximum iteration	100
	Stopping criteria	Maximum number of iteration
GP	Minimum improvement	$1e-5$
	Input membership function	gauss, trip, trap, and gauss2
	Output membership function	Linear
	Number of input membership function	2
	Number of rules	8

**Fig. 2** The antimicrobial study of WNS-CH on *Bacillus subtilis* and *Klebsiella pneumoniae*



resulting in cell lysis occurs by the adsorbent-cell membrane interaction involving the interference of the adsorbent with cell replication, thus damaging the cell membrane and DNA of the cell [45]. This shows that WNS-CH has the potential for bio applications in water purification to act as a biofilter for the removal of the *Bacillus subtilis* and *Klebsiella pneumoniae*.

### 3.2 Scanning Electron Microscopy analysis

The SEM micrograph of the adsorbents; WNS, WNS-CH, and  $Pb^{2+}$ -loaded WNS-CH are shown in Fig. 3a–c, respectively. The micrograph of WNS shows an irregular hollow shape with a spongy surface prior functionalizing WNS with CH. Marked observable changes in the surface of WNS were noticed after functionalization with CH which showed a homogenous well-organized regular hollow ellipsoidal morphology. Comparing Fig. 3a, b shows that CH was effective in producing biosorbent with higher porosity. The pores formed as a result of functionalization were wider and developed more uniformly. This was attributed to the effective physiochemical activation in removing volatile component(s) and tarry materials that blocked the pores. Based on the pore sizes, it can be said that WNS-CH demonstrated heterogeneous pores which is requisite for effective uptake of  $Pb^{2+}$  ions, upon comparing the micrograph of WNS-CH composite shown in 3b with  $Pb^{2+}$ -loaded WNS-CH (Fig. 3c) after absorption. A change in the morphology of  $Pb^{2+}$ -loaded WNS-CH was observed which could be attributed to the influx of Pb II ions thus resulting to its adsorption on the surface of the bio sorbent, thereby depicting the blockage of the well-organized hollow channel.

### 3.3 Fourier transform infrared (FTIR)

The FTIR analyses provided spectra and the detailed surface chemistry of the adsorption and the corresponding mechanism of adsorption of  $Pb^{2+}$  onto WNS-CH loaded WNS-CH composite which was prepared from the native WNS. Figure 4 presents detailed band information of the

WNS and WNS-CH composites WNS-CH+  $Pb^{2+}$ , and the corresponding band assignments are presented in Table 2. The FTIR spectra showed some typical absorption band ranges as presented in Table 2. This includes the native WNS and WNS-CH composite at  $3570\text{--}3200\text{ cm}^{-1}$  and  $3400\text{--}3380\text{ cm}^{-1}$  which are assigned to the hydroxyl, amino, and carbonyl groups, respectively. The observed band shift in the spectra of the composite suggests that modification has taken place, thereby leading to the structure and functional changes/rearrangements owing to the presence of chitosan on the walnut. The significant changes in FTIR spectra resulted in band shifting or broadening, thus confirming the modification effects in creating structural changes in WNS-CH in comparison with WNS.

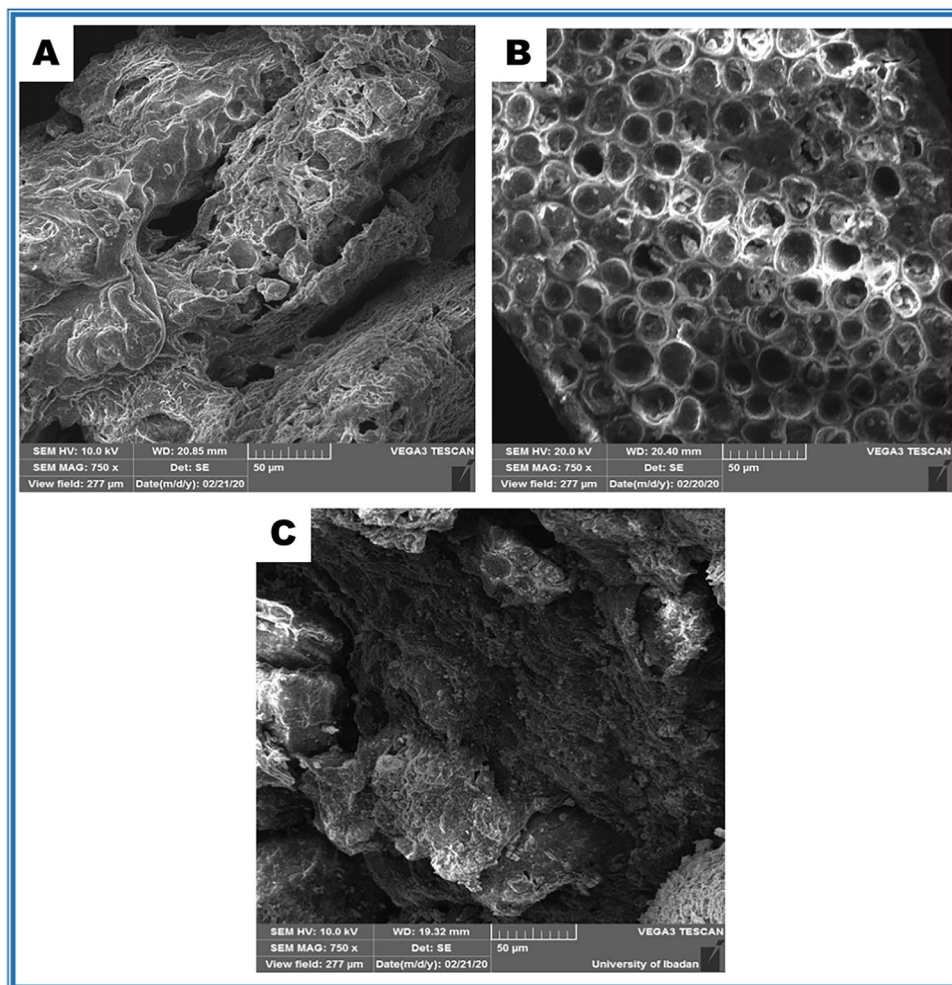
As seen in Table 2, the negatively charged functional groups of O-H (hydroxyl) were observed to promote the biosorption process of positively charged  $Pb^{2+}$  ions and the disinfection of microbes onto WNS-CH [46]. Upon comparing the FTIR result of Pb II ion-loaded composite WNS-CH and with WNS-CH prior absorption, an observed change that corresponds to shift in the absorption bands of the analyzed functional groups was observed. The majority of the functional group of the Pb II ion-loaded composite WNS-CH were observed to have shifted to a lower absorption band. Only the ester moiety was observed to increase as shown in Table 2. This phenomenon is, however, attributed to the interactions of the Pb ions with the functional groups of the composite. This is due to the functional group's high reactivity, thus resulting in their respective deprotonation. This was in agreement with previous functionalization studies on the other adsorbents reported [47, 48]. This, however, corroborated the SEM result due to the formation of a well-defined regular porous surface. The synergistic effect resulted in the provision of more functional groups available for metal binding, thereby facilitating its rapid uptake from their respective solutions.

### 3.4 Kinetic analysis

Table 3 shows various kinetic parameters for each model, and Fig. 5 shows the kinetic model plots used in studying



**Fig. 3** The Scanning Electron Microscopy of **a** walnut shell (WNS), **b** chitosan functionalized walnut shell (WNS-CH) composite, and **c** WNS-CH after adsorption of  $Pb^{2+}$



the adsorption-time relationship of the adsorption process. Figure 5 shows that uptake of  $Pb^{2+}$  significantly increased firstly and changed slowly with time until adsorption equilibrium was reached (0–60 mins). This is assumed to result from higher availability of vacant pores on the adsorbent and a larger concentration gradient, resulting in adsorption speed. Based on correlation coefficient ( $R^2$ ) obtained for all three kinetic models, namely, PFOM, PSOM, and Elovich. It was observed that the  $R^2$  values for all models were close to unity, whereas, based on the error values, PSOM had the lowest error value of 0.1389. This indicates that the removal could be best fitted to PSOM model with  $R^2 = 0.9674$ . This shows that the exchange or sharing of electrons between the adsorbent and the adsorbate is the rate limiting step, thus suggesting chemisorption. It is assumed that  $Pb^{2+}$  species are likely moved from the bulk solution into the solid phase through an intraparticle diffusion process.

*PSOM* pseudo-second-order model, *PFOM* pseudo-first-order model, Elovich model

### 3.5 Isothermal analysis

Nonlinear forms of four theoretical models were used to test the experimental isotherm data obtained, namely, the Brouers-Sotolongo, Freundlich, Langmuir, and Temkin models. Figure 6 shows the isotherm plots of  $Pb^{2+}$  onto WNS-CH, and the respective isotherm parameters of each plot are presented in Table 4. With respect to close comparison of coefficient of determination ( $R^2$ ), error values, and other parameters for all the isotherms, it can be deduced that the adsorption of  $Pb^{2+}$  onto WNS-CH is best fitted to the Brouers-Sotolongo ( $R^2 = 0.9506$ , error= 2.4289) and Langmuir ( $R^2 = 0.9509$ , error= 1.8104) isotherm models, with a marginal difference between the predicted parameters for both models. According to the Brouers-Sotolongo adsorption capacity of WNS-CH for  $Pb^{2+}$  is predicted to be  $\approx 371$  mg  $Pb^{2+}$ /every g of WNS-CH. This isotherm assumes that WNS-CH has a homogeneous surface that contains sites with same energy resulting in complete monolayer adsorption of  $Pb^{2+}$ . The theoretical  $Q_m$  value of 370.5838

**Fig. 4** The FTIR spectra of **a** WNS, **b** WNS-CH composite, and **c** lead-treated WNS-CH composite

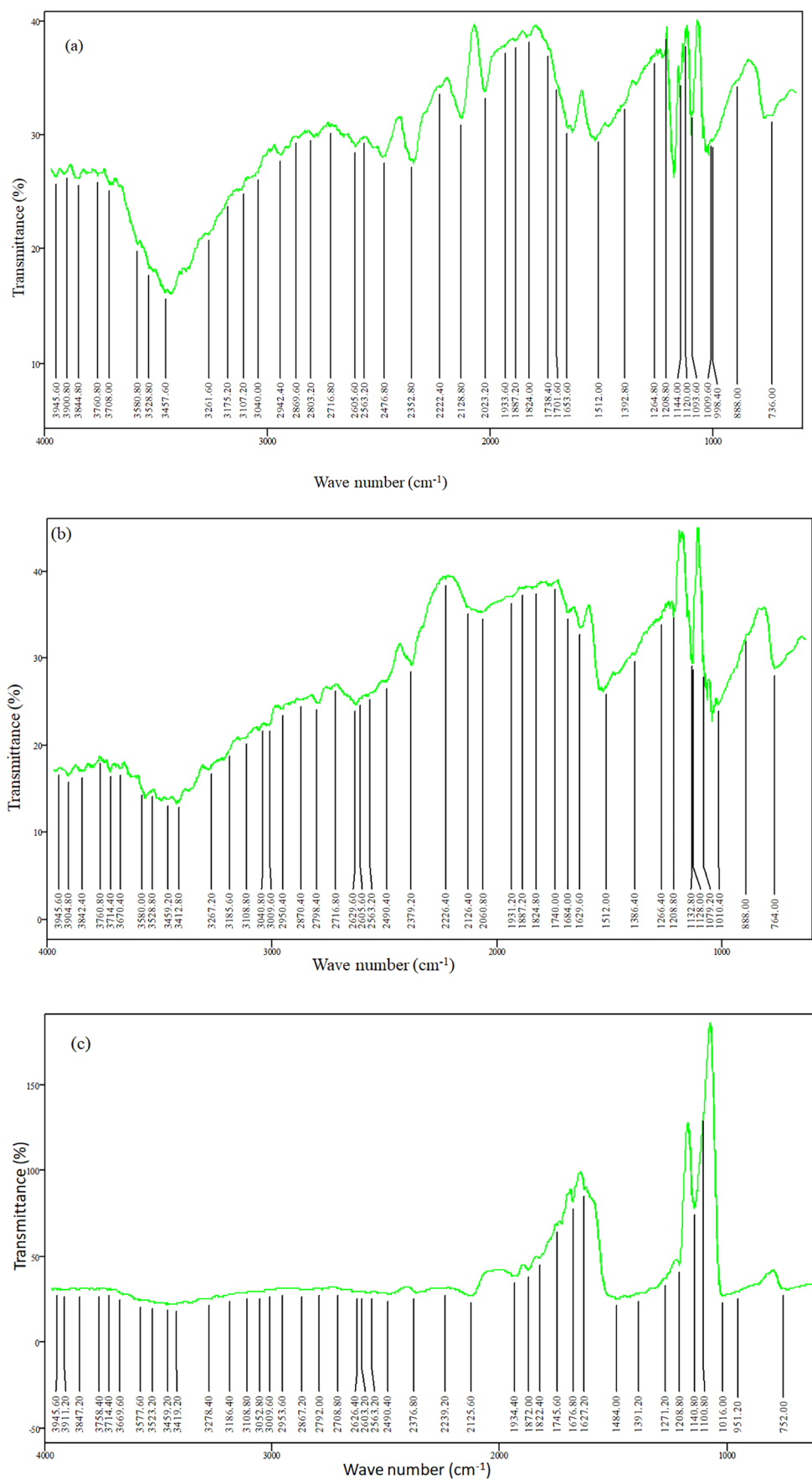


**Table 2** FTIR peaks and their corresponding functional groups

Native WNS (cm <sup>-1</sup> )	WNS-CH (cm <sup>-1</sup> )	Pb <sup>2+</sup> + WNS-CH (cm <sup>-1</sup> )	Assignment
3760	3760	3758	O-H & N-H groups
3557	3580	3523	
3457	3412	3544	
1653	1629	1620	Amine, bending
1093	1979	1016	C-N, amine
1208	1208	1208	C-O stretch
2803	2798	2792	N-CH <sub>3</sub>
1738	1740	1745	Ester
888	888	–	NH <sub>3</sub> rocking vibration

**Table 3** Various predicted kinetic data for the adsorption of Pb<sup>2+</sup> on the adsorbent

PFOM		
R <sup>2</sup>	SE	Parameters
0.9674	0.1582	Q <sub>e</sub> = 6.0493 (mg/g); K <sub>1</sub> = 0.4568 (min <sup>-1</sup> )
PSOM		
R <sup>2</sup>	SE	Parameters
0.9674	0.1389	Q <sub>e</sub> = 6.0422 (mg/g); K <sub>2</sub> = 3276.1204 (g/mg min <sup>-1</sup> )
Elovich		
R <sup>2</sup>	SE	Parameters
0.9644	0.1512	B = 3.9951 (mg/g); α = 1.2E008 (mg/gmin <sup>-1</sup> )

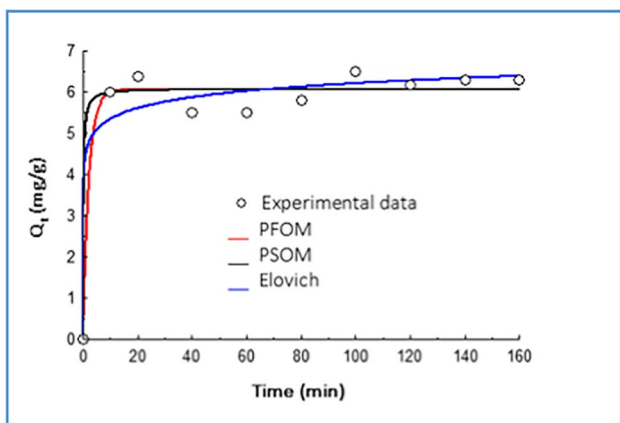


**Fig. 5** Kinetic model plots for the adsorption of Pb<sup>2+</sup> onto the WNS-CH adsorbent

mg/g obtained for BS showed a good fit with an R<sup>2</sup> value of 0.9506, while Langmuir showed an adsorption capacity of WNS-CH with Q<sub>m</sub> value ≈ 14 mg/g and least R<sup>2</sup> value of 0.8712 compared to the other isotherm as presented in Table 4. The separation factor (R<sub>L</sub>) is an important Langmuir parameter which tells about the favorability (favorable: (0 < R<sub>L</sub> < 1)) of adsorption which was used to evaluate

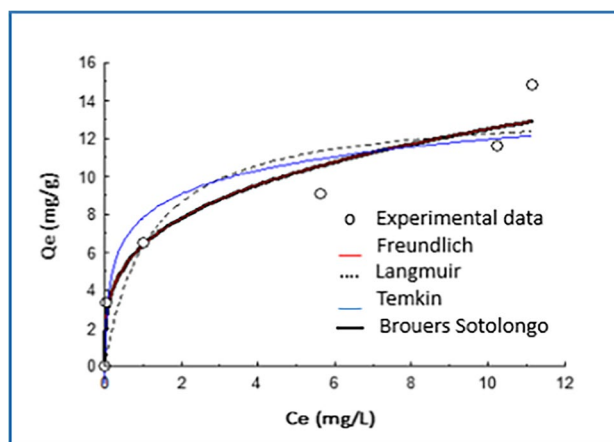


**Fig. 6** Isotherm plots for the adsorption of Pb<sup>2+</sup> on WNS-CH

the adsorption process. In the concentration range studied (20–100 mg/L), the recorded R<sub>L</sub> value is 0.85700 thus suggesting a favorable adsorption in the Pb<sup>2+</sup>-WNS-CH system. Similar study for Pb<sup>2+</sup> was reported by [49]. The Brouer-Sotolongo model assumes the presence of heterogenous active sites on the surface of WNS-CH adsorbent with equal energy responsible for uptake of Pb<sup>2+</sup>.

More so, the heterogeneity factor (n) of Freundlich model can be used to indicate the degree of favorability of adsorption [50, 51]. The Freundlich constant (n ≈ 3) (Table 4) shows a highly favorable adsorption of Pb<sup>2+</sup> on the surface of the WNS-CH [9].

### 3.6 Mechanism of Pb<sup>2+</sup> ion removal

A marked difference was observed in the FTIR spectra of the adsorbent (WNS-CH) before and after adsorption of the metal ions as shown in Fig. 4a–c. As shown in Table 2, the metal-loaded WNS-CH appeared at 1320–1210 cm<sup>-1</sup>, which was attributed to the carbonyl groups. After the interaction of the metal ions with the adsorbents, a decrease in the O-H absorption band of Pb<sup>2+</sup>-WNS-CH was observed at 3523 cm<sup>-1</sup> compared to WNS-CH at 3580 cm<sup>-1</sup>. Furthermore, the same trend was observed in the C-N absorption band, in which a decrease in the C-N absorption band of Pb<sup>2+</sup>-WNS-CH at 1016 cm<sup>-1</sup> was noticed compared to WNS-CH at 1079 cm<sup>-1</sup> as shown in Table 2. The observed C-N absorption also corresponds to the observed vibrational frequency of the methylamino group (>N-CH<sub>3</sub>) in which a blue shift was observed in the vibrational frequency of Pb<sup>2+</sup>-WNS-CH 2782 cm<sup>-1</sup> as against WNS-CH at 2798.

Furthermore, the wavenumber range 3270–3540 cm<sup>-1</sup> corresponds to the internal bonded O-H stretch. However, an interhydrogen bonding vibrational shift to 3544 and 3523 cm<sup>-1</sup> was observed in Pb<sup>2+</sup>-WNS-CH compared

**Table 4** Adsorption isotherm data for the adsorption of  $\text{Pb}^{2+}$  on to WNS-CH adsorbent

Models	$R^2$	Error	Parameters
Brouers-Sotolongo	0.9506	2.4289	$Q_m = 370.5838 \text{ mg/g}$ ; $k_w = 0.0173$ ; $\alpha = 0.2955$
Freundlich	0.9509	1.8104	$K_F = 6.3623 \text{ (mg g}^{-1}) \text{ (Lmg}^{-1})^{1/n}$ ; $n = 3.4173$
Langmuir	0.8712	4.7526	$Q_m = 13.6589 \text{ mg/g}$ ; $k_L = 0.85700$
Temkin	0.9118	3.2548	$\beta = 1.7947 \text{ J/mg}$ ; $\alpha = 77.5389 \text{ L/g}$

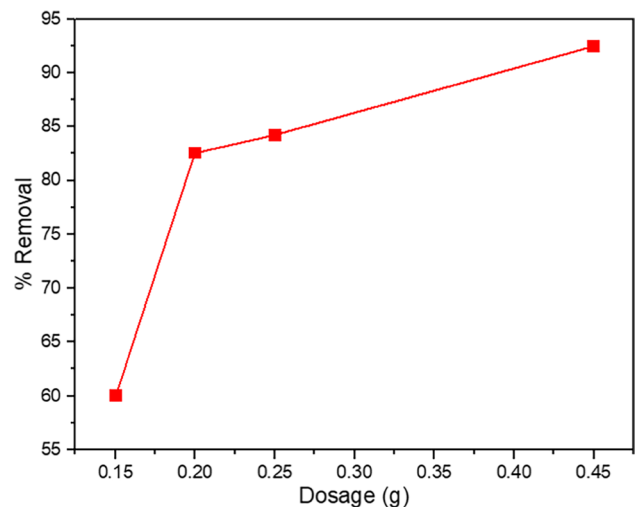
to the  $3580 \text{ cm}^{-1}$  observed in WNS-CH. Also, an  $\text{NH}_3$  rocking vibration noticed in WNS-CH with wavenumber  $876 \text{ cm}^{-1}$  was absent in  $\text{Pb}^{2+}$ -WNS-CH compared as shown in Table 2, indicating that adsorption has successfully taken place. This band disappearance can be translated to the open pore in WNS-CH becoming occupied and trapped by the  $\text{Pb}^{2+}$  during the sorption process resulting in the unavailability of surface functional groups for further interaction of the WNS-CH with  $\text{Pb}^{2+}$ . Albeit, the observed changes in the intensity of adsorption and the wavenumber of functional groups strongly validate the occurrence of complexation between nitrogen and oxygen atoms on the adsorbent binding sites and the metal ions. However, from the FTIR spectra, it is suggested that the maximum uptake of lead ions from their respective solutions by the WNS-CH composite is due to the availability of more number of N and O atoms.

In addition, the observed SEM micrograph after adsorption with  $\text{Pb}^{2+}$  +loaded composite showed a uniform but seems blocked (i.e., occupied) surface with fiber-like features compared to WNS and WNS-CH which could be suggested to be due to adsorption of the metal ( $\text{Pb}^{2+}$ ) ion become trapped by the adsorbents. This can be further corroborated with the kinetic plot that the sorption process becomes less competitive as the process approaches steady-state equilibrium

### 3.7 Effects of process variables on adsorption of $\text{Pb}^{2+}$

#### 3.7.1 Effect of adsorbent dose

Figure 7 shows the result of  $\text{Pb}^{2+}$  uptake profile versus the adsorbent dose. The dosage varied from 0.15–0.45 g, keeping all other operating variables constant. As illustrated in Fig. 5, the percentage uptake of  $\text{Pb}^{2+}$  is observed to increase from 60% to 92.5% as the dosage of adsorbents increases. This may result from increased available active sites on the WNS-CH surface area as the dosage increases. This is similar to other studies that have reported metal removal efficiency increased with increasing adsorbent dosage as a result of more adsorptive sites on adsorbent surfaces [52]. The optimum dose for this study is 0.45 g.

**Fig. 7** Effect of adsorbent dose on the adsorption of  $\text{Pb}^{2+}$  onto the WNS-CH adsorbent

#### 3.7.2 Effect of pH

Purification of wastewater using adsorbents has been discovered to be highly pH-dependent, majorly acidity, since this may greatly influence the adsorbent charged surface and the degree of ionization of various pollutants. In this study, pH was varied between 3 and 10 and investigation revealed 58% as minimum uptake of  $\text{Pb}^{2+}$  at pH 3.0, which further increased with increasing pH (Fig. 8). The pH 10 was found as the optimum pH with maximum adsorption efficiency of 94%. It is assumed that lower adsorption occurred at low pH which may be due to the competition for active sites between the  $\text{H}^+$  and  $\text{Pb}^{2+}$  and could also cause restriction in dissociation of carboxyl group on WNS-CH surface. On the other hand, as pH increases, more functional groups became available for  $\text{Pb}^{2+}$  adsorption, resulting in a reduction in  $\text{H}^+$  concentrations and subsequently enhanced adsorption. It can be suggested that the adsorption of  $\text{Pb}^{2+}$  is unfavorable at lower pH (acidic).

Other researchers have reported similar findings on the effects of pH on heavy metal removal using various carbonaceous sorbents [19, 53]. It can also be assumed that the WNS-CH surface becomes positively charged at lower pH values, leading to electrostatic repulsion, thereby making  $\text{Pb}^{2+}$  more difficult to be adsorbed unto the surface.

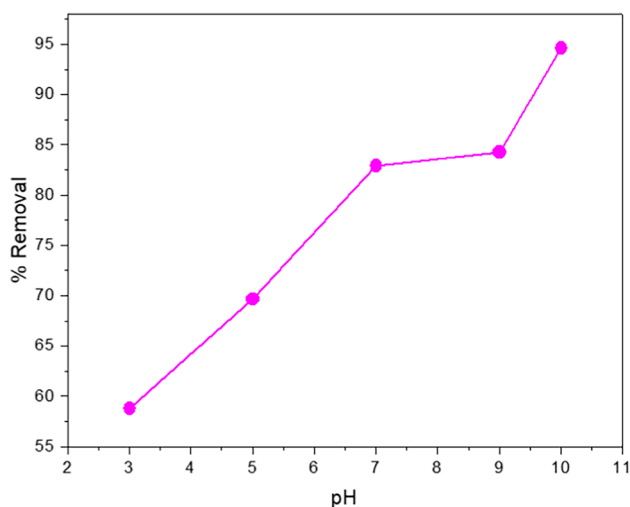


**Fig. 8** Effects of pH on the adsorption of Pb<sup>2+</sup> onto the WNS-CH adsorbent

Contrarily, at higher pH value, WNS-CH surface becomes negatively charged, and more active adsorption sites are available, leading to higher adsorption as a result of electrostatic attraction between active sites and Pb<sup>2+</sup>.

### 3.7.3 Effect of temperature

The results in Fig. 9 demonstrate that Pb<sup>2+</sup> uptake tends to increase slightly from 20 °C to 40 °C showing better adsorption at a higher temperature, which is an endothermic process. An increase in temperature may result in a swelling effect within the internal structure of the adsorbents, which enables more Pb<sup>2+</sup> penetration [14, 54]. An increase in kinetic energy of adsorbent with an increase in temperature is assumed to be responsible for enhanced

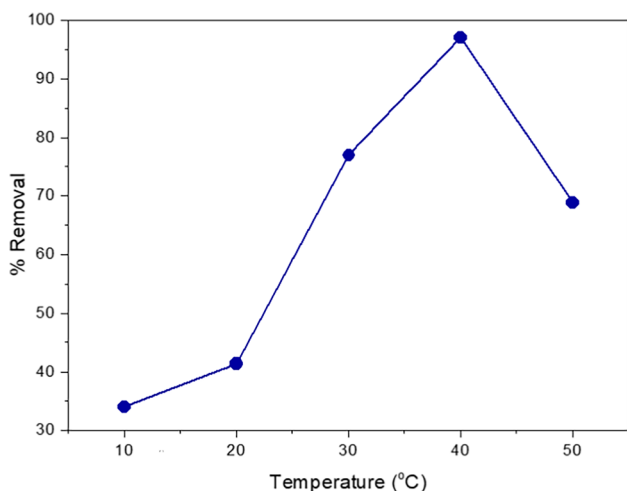


**Fig. 9** Effect of temperature on the adsorption of Pb<sup>2+</sup> onto the WNS-CH adsorbent

adsorption efficiency. Secondly, at a higher temperature, there is bond rupture of functional groups on the adsorbent surface, and this could lead to an increase in the number of active sites on the adsorbents, which in turn could lead to an increase in adsorption with the rise in temperature [14, 15]. The optimum temperature for the process is 40 °C with 97.07% adsorption capacity. From the temperature of 40–50 °C, a slight decrease in the adsorption of Pb<sup>2+</sup> was observed, which may be due to weakening of the physical bonds between the adsorbate molecules and the active site of the adsorbent at an extremely higher temperature.

### 3.7.4 Thermodynamics studies for the adsorption of Pb<sup>2+</sup> on to WNS-CH adsorbent

Tables 5 show the thermodynamic parameters for the adsorption of Pb<sup>2+</sup> unto WNS-CH. The ΔG° values at all temperature considered were all negative. In addition, the ΔG° values are observed to decrease with an increase in temperature. Furthermore, positive ΔH° and ΔS° values were obtained. The results indicate that the adsorption process is endothermic and indicating that the uptake of Pb<sup>2+</sup> on the surface of the adsorbent is spontaneous [55].

### 3.8 Performance metrics of the neuro-fuzzy model

The neuro-fuzzy model has a merit of computational flexibility and framework which allows variation of its hyperparameters to achieve optimality in the model [56]. Sequel to the significant effect of the control parameters of the clustering on the performance of neuro-fuzzy models, this study tested the ANFIS model clustered with the GP and FCM with their varying hyperparameters. Shown in Table 6 is the performance metrics of FCM-ANFIS models with cluster numbers 2–8. The computational time of all submodels is also presented in Table 5. The performance in the FCM-clustered ANFIS model followed a similar trend as the cluster number increases from 2 to 8 with marginal variation across all metrics. Based on the RMSE values, the performance of the FCM-clustered model is in the following order: FCM – ANFIS<sub>2</sub><sub>RMSE=1.353</sub> > FCM – ANFIS<sub>8</sub><sub>RMSE=1.355</sub> > FCM – ANFIS<sub>1</sub><sub>RMSE=1.445</sub> > FCM – ANFIS<sub>4</sub><sub>RMSE=1.532</sub> > FCM – ANFIS<sub>5</sub><sub>RMSE=1.543</sub> > FCM – ANFIS<sub>3</sub><sub>RMSE=1.563</sub> > FCM –

**Table 5** Thermodynamics table for the adsorption of Pb<sup>2+</sup> on to WNS-CH adsorbent

	283 K	293 K	303K	313K	323 K
ΔG° (kJ·mol <sup>-1</sup> )	-38.715	-40.702	-42.689	-44.676	-46.663
ΔH° (kJ·mol <sup>-1</sup> )	+17.517				
ΔS° (J·mol <sup>-1</sup> ·K <sup>-1</sup> )	+190.704				

**Table 6** Performance metrics outcome of the FCM-clustered ANFIS models

Submodel	Number of cluster	Performance metrics				
		RMSE	MAD	MAPE	R <sup>2</sup>	CT (secs)
FCM-ANFIS1	2	1.445	0.645	3.454	0.9902	5.34
FCM-ANFIS2	3	1.353	0.632	2.983	0.9911	5.64
FCM-ANFIS3	4	1.563	0.703	3.485	0.9893	5.74
FCM-ANFIS4	5	1.532	0.693	4.243	0.9923	5.71
FCM-ANFIS5	6	1.543	0.734	4.164	0.9833	5.53
FCM-ANFIS6	7	1.743	0.787	4.674	0.9873	5.72
FCM-ANFIS7	8	1.355	0.735	5.012	0.9736	5.26

ANFIS7<sub>RMSE=1.7435</sub>. Considering a minimum MAPE value of 2.983 (FCM – ANFIS2<sub>Cluster number=3</sub>) and maximum of 5.012 (FCM – ANFIS7<sub>Cluster number=8</sub>), the accuracy of all the FCM-ANFIS model is in the range 95.09 % to 97.12 % at the testing phase. These values are reasonable as it depicts acceptable fit between the experimental and predicted values of Removal rate. Above cluster number 8, no significant improvement was observed in the performance but rather a decline in performance with uncertainty, overfitting, and noise [57]. Based on minimum error criteria, the best FCM-clustered ANFIS model was obtained at cluster number 3 (FCM-ANFIS2) with RMSE, MAD, MAPE, and R<sup>2</sup> values of 1.046, 0.514, 1.645, and 0.9956, respectively, at the training phase and 1.353, 0.632, 2.983 and 0.9911, respectively, at the testing phase. The lowest RMSE and MAD values of the FCM-ANFIS2 depicts the reliability and eligibility of the model in predicting the removal rate of Pb<sup>2+</sup> onto the WNS-CH adsorbent. The model is 97.12 % accurate (MAPE=2.983), representing the strongest agreement between the experimental and predicted removal rate of Pb<sup>2+</sup> onto the WNS-CH adsorbent.

Table 7 represents the evaluation outcomes of the GP-clustered ANFIS model based on the selected metrics. The GP technique tested four input membership function types based on their prominent applications in previous studies [34]. A close-range performance was observed in all the submodels based on the GP clustering with marginal discrepancies. Based on RMSE values, the performance of the GP-ANFIS models is in the order GP – ANFIS2<sub>triMF</sub> > GP – ANFIS1<sub>gaussMF</sub> > GP – ANFIS4<sub>gauss2MF</sub> > GP – ANFIS3<sub>trapMF</sub>. Based on the MAPE values, the accuracies of the models were in the following order: GP – ANFIS2<sub>triMF</sub> (98.31%) >

GP – ANFIS1<sub>gaussMF</sub> (97.35%) > GP – ANFIS3<sub>trapMF</sub> (97.32%) > GP – ANFIS2<sub>gauss2MF</sub> (96.76%). The triMF gave the best outcome with the lowest prediction error and highest accuracy. Owing to the computational intensity of the grid partitioning techniques based on a large rule base, the computational time is an metrics for evaluating its performance [58]. The GP-ANFIS recorded higher computational time than the FCM-ANFIS model. Comparatively, it was observed that there was a trade-off in the computational time and accuracy of all the GP-ANFIS, as it gives a more accurate result than the FCM-clustered model which computed in lesser time. The overall best model was obtained with the GP-ANFIS model with triangular membership function (triMF) with the following statistical metrics values: RMSE<sub>triMF</sub> = 1.217, MAD<sub>triMF</sub> = 0.563, MAPE<sub>triMF</sub> = 1.698 and R<sup>2</sup><sub>triMF</sub> = 0.9966. The RMSE and MAD values of the GP – ANFIS2 depicts the reliability and eligibility of the model in predicting the removal rate of Pb<sup>2+</sup> onto the WNS-CH adsorbent while its accuracy of 98.31 % depicts an excellent agreement in the experimental and predicted removal rate.

Figures 10 and 11 represent the comparison plot of experimental and predicted removal rate values using the best FCM-ANFIS and GP-ANFIS model at the training and testing phase, respectively. The figures show a strong agreement between the experimental data and the predicted values with a very less misprediction. A similar trend exists between the predicted and experimental data for both optimal FCM-ANFIS and GP-ANFIS, giving the best prediction outcomes.

The regression plot of the best FCM-ANFIS and GP-ANFIS model is presented in Figs. 12 and 13. It is revealed that the experimental and predicted removal rate Pb<sup>2+</sup> onto the WNS-CH adsorbent had the best GP-ANFIS and

**Table 7** Performance metrics outcome of the FCM-clustered ANFIS models

Submodel	Membership function	Performance metrics				
		RMSE	MAD	MAPE	R <sup>2</sup>	CT (secs)
GP-ANFIS1	gaussMF	1.324	0.585	2.654	0.9945	8.54
GP-ANFIS2	triMF	1.217	0.563	1.698	0.9966	8.74
GP-ANFIS3	trapMF	1.421	0.604	2.683	0.9953	8.95
GP-ANFIS4	gauss2MF	1.336	0.592	3.246	0.9962	8.81

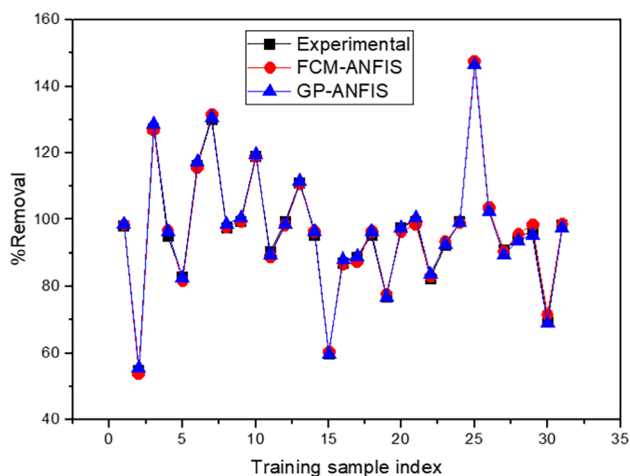


Fig. 10 Comparison plot of the experimental and predicted removal rate of Pb<sup>2+</sup> onto the WNS-CH adsorbent at the training phase

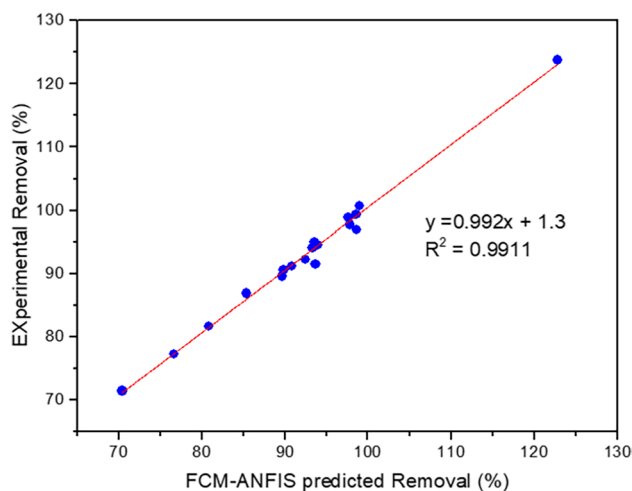


Fig. 12 Regression plot of the experiment and the FCM-ANFIS predicted removal rate of Pb<sup>2+</sup> onto the WNS-CH adsorbent

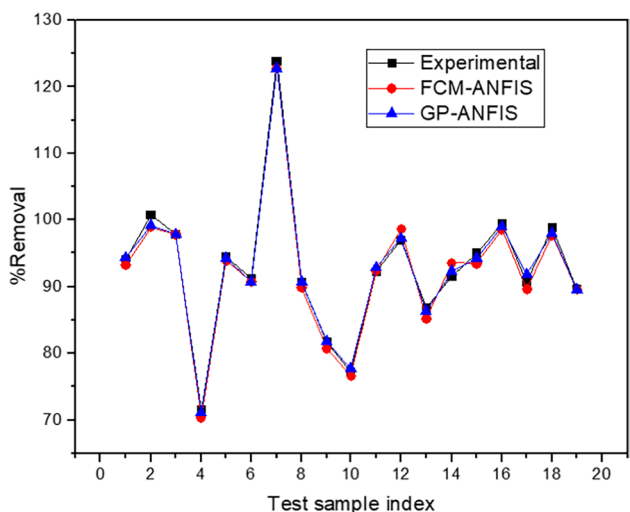


Fig. 11 Comparison plot of the experimental and predicted removal rate of Pb<sup>2+</sup> onto the WNS-CH adsorbent at the testing phase

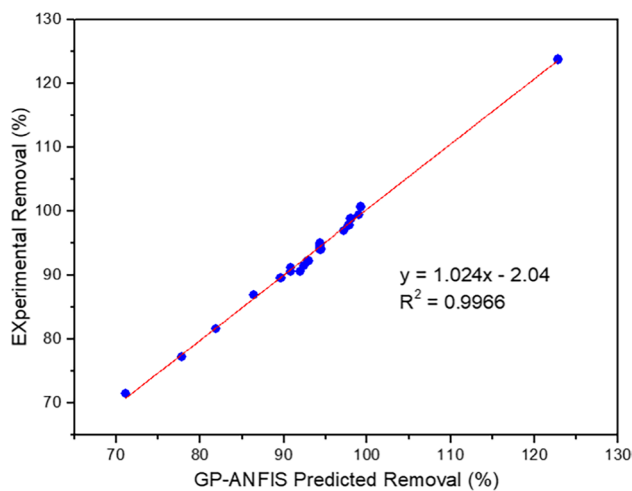


Fig. 13 Regression plot of the experimented and the GP-ANFIS predicted removal rate of Pb<sup>2+</sup> onto the WNS-CH adsorbent

FCM-ANFIS had the highest density point clustering around zero while low density of data is far away from the origin which means that the model provides a good fit to the data.

### 3.9 Comparison of the present study with previous works on Pb<sup>2+</sup> adsorption

WNS-CH was observed to compare favorably in terms of strength and adsorptive capacity with other biomass-derived or synthesized adsorbents used for the removal of lead ions from the aqueous phase documented in the literature as presented in Table 8. Furthermore, WNS-CH in this study shows a better performance with excellent percentage

sorption capacity (>90%) compared to earlier reported studies [19, 50, 61] as shown in Table 8.

### 3.10 Cost analysis

The price difference (cost analysis) between WNS-CH and commercial activated carbon (CAC) is shown in Table 9. This recorded a simple proof that WNS-CH is very cheap than CAC. According to the table, the total cost of purchasing 1 kg of CAC (with transportation fee) was estimated at 392.50 USD, while the total cost recorded for the preparation, with the chitosan (1 kg) used for modifying the WNS, transportation to filtration and cost of energy supplied. The electricity bill recorded a total value of 131.57 USD, while chitosan was observed to account for the most significant

**Table 8** Comparison of the sorption capacity value of Pb<sup>2+</sup> using different adsorbents

$\frac{s}{n}$	Adsorbent	Adsorbate	Adsorption capacity/percentage removal	Equilibrium models	References
1	Sewage sludge and bagasse were	Pb <sup>2+</sup>	135.54 mg/g	Langmuir and Freundlich	[59]
2	Callinectes sapidus biomass	Pb <sup>2+</sup> , cadmium, and nickel ion	31.44 mg/g, 29.23 mg/g, and 29.15 mg/g	Langmuir and Freundlich	[20]
3	Novel porous bentonite- and calcite-biochar composite	Pb <sup>2+</sup>	99.9%	-	[60]
4	Polypyrrole-based activated carbon	Pb <sup>2+</sup>	50 mg/g	Langmuir and Freundlich	[51]
5	Sawdust	Pb <sup>2+</sup>	2.4 mg/g	Langmuir and Freundlich	[61]
6	Cucumber peel	Pb <sup>2+</sup>	133.60 mg/g	Langmuir, Freundlich and Temkin	[62]
7	Metal-organic framework MIL-100(Fe)	Pb <sup>2+</sup> and Chromium	22.86 mg/g and 30.45 mg/g	Sips, Temkin, Freundlich, and Langmuir	[63]
8	Waste vinasse	Pb <sup>2+</sup>	1.007 mmol/g	Freundlich, Langmuir, and Dubinin-Radushkevich (D-R)	[19]
9	Raffia palm	Pb <sup>2+</sup>	72.62 mg/g	Langmuir, Freundlich, Temkin, and Dubinin-Radushkevich	[64]
10	MoS <sub>2</sub> -clinoptilolite	Pb <sup>2+</sup>	3.45 mg/g	Freundlich, and Langmuir	[50]
10	Chitosan-walnut composites (WNS-CH)	Pb <sup>2+</sup>	6.36 mg/g (>90%)	Langmuir, Freundlich, Brouers Sotolongo, and Temkin	<i>This study</i>

**Table 9** Price difference between WNS-CH and CAC

Cost description	Price (US \$)	
	WNS-CH (1 kg)	CAC (1 kg)
Transportation	–	12.00
Chitosan	120	–
Wall nut shell	–	–
Deionized water	7.35	–
Filter paper	2.5	–
Electricity	1.72	–
Cost of purchase	–	380.50
Total	131.57	392.50
Difference (CAC–WNS-CH)	260.93	

cost in the production of the adsorbent as presented in Table 9. However, the adsorbent is far cheaper than CAC, suggesting the consideration of the composite use in the study as an alternative for CAC.

## 4 Conclusion

The study assessed the use of walnut shell and chitosan as suitable precursors for the preparation of a composite material (WNS-CH) with great potentials for Pb<sup>2+</sup> uptake from aqueous solution vis-à-vis its antimicrobial activity on

*Bacillus subtilis* and *Klebsiella pneumoniae*. It was observed that the adsorption of Pb<sup>2+</sup> increased with an increased in temperature, pH, and adsorbent dosage. Adsorption efficiency of 94 % was obtained under the conditions of initial pH 10, dosage 45 mg, and temperature of 40 °C. The thermodynamic parameters revealed that the adsorption process is spontaneous and endothermic in nature. Equilibrium data were well explained by Freundlich isotherm with  $R^2 = 0.9509$  indicating a multilayer adsorption, while pseudo-first-order kinetics was best fit for the kinetic data with an  $R^2$  value of 0.9674 at a  $q_e$  value of 6.0493 mg/g. WNS-CH showed a biopotency against *Bacillus subtilis* and *Klebsiella pneumoniae* with a mean ZI of  $5.3 \pm 1.16$  and  $6.0 \pm 1.00$ . The SEM and FTIR showed a well-organized hollow channel, with O-H, N-H, C-N, and C-O functional groups which are responsible for the adsorption process as evident in the morphological restructuring and changes in the IR bands.

Lastly, a study involving cost-effective machine learning models revealed that GP-clustered ANFIS model (with RMSE = 1.217, MAD = 0.563, MAPE = 1.698, and  $R^2 = 0.9966$  at the testing phase) is an effective model tool for predicting the adsorption process based on the input of relevant parameters. The findings of this study show WNS-CH composite as an inexpensive dual purpose adsorbent system: biosorbent and biofilter. Albeit, further modifications of WNS-CH are necessary to enhance its adsorption capacity and subsequent work should extend



the application of WNS-CH into practical application with associated regeneration.

**Acknowledgements** All authors acknowledge their universities for the enabling platform to carry out this research. Kayode Adesina Adegoke acknowledges the Global Excellence Stature (GES) 4.0 Postdoctoral Fellowships Fourth Industrial Revolution and the University of Johannesburg, South Africa.

**Availability of data and materials** All data and materials used in this study are available within this article.

**Author contribution** A. Bamisaye: conceptualization, investigation, methodology, validation, visualization, writing—original draft preparation, writing—review, and editing. M. O. Adesina, M. O. Alfred, M. A. Idowu, and Oluwatobi Adeleke: investigation, validation, visualization, and writing—original draft preparation. K. A. Adegoke: investigation, data curation, validation, visualization, writing—review, and editing and supervision. All authors read and approved the manuscript.

**Funding** Open access funding provided by University of Johannesburg.

## Declarations

**Ethics approval and consent to participate** This article does not contain any studies involving human or animal subjects.

**Competing interest** The authors declare no competing interests.

**Open Access** This article is licensed under a Creative Commons Attribution 4.0 International License, which permits use, sharing, adaptation, distribution and reproduction in any medium or format, as long as you give appropriate credit to the original author(s) and the source, provide a link to the Creative Commons licence, and indicate if changes were made. The images or other third party material in this article are included in the article's Creative Commons licence, unless indicated otherwise in a credit line to the material. If material is not included in the article's Creative Commons licence and your intended use is not permitted by statutory regulation or exceeds the permitted use, you will need to obtain permission directly from the copyright holder. To view a copy of this licence, visit <http://creativecommons.org/licenses/by/4.0/>.

## References

1. Das SK, Ghosh GK, Avasthe R (2021) Conversion of crop, weed and tree biomass into biochar for heavy metal removal and wastewater treatment. *Biomass Convers Biorefinery*. <https://doi.org/10.1007/s13399-021-01334-y>
2. Wang D, Luo W, Zhu J et al (2021) Potential of removing Pb, Cd, and Cu from aqueous solutions using a novel modified ginkgo leaves biochar by simply one-step pyrolysis. *Biomass Convers Biorefinery*. <https://doi.org/10.1007/s13399-021-01732-2>
3. Shah N, Khisroon M, Shah SSA (2020) Assessment of copper, chromium, and lead toxicity in fish (*Ctenopharyngodon idella* Valenciennes, 1844) through hematological biomarkers. *Environ Sci Pollut Res Int* 27:33259–33269. <https://doi.org/10.1007/s11356-020-09598-z>
4. Eletta OAA, Ayandele FO, Ighalo JO (2021) Adsorption of Pb(II) and Fe(II) by mesoporous composite activated carbon from *Tithonia diversifolia* stalk and *Theobroma cacao* pod. *Biomass Convers Biorefinery*. <https://doi.org/10.1007/s13399-021-01699-0>
5. Wani AL, Ara A, Usmani JA (2015) Lead toxicity: a review. *Interdiscip Toxicol* 8:55–64. <https://doi.org/10.1515/intox-2015-0009>
6. Guo W, Pan B, Sakkiyah S et al (2019) Persistent organic pollutants in food: contamination sources, health effects and detection methods. *Int J Environ Res Public Heal* 16:4361
7. Ahsan MA, Islam MT, Hernandez C et al (2018) Biomass conversion of saw dust to a functionalized carbonaceous materials for the removal of tetracycline, sulfamethoxazole and bisphenol A from water. *J Environ Chem Eng* 6:4329–4338. <https://doi.org/10.1016/j.jece.2018.06.040>
8. Wilkinson J, Hooda PS, Barker J et al (2017) Occurrence, fate and transformation of emerging contaminants in water: an overarching review of the field. *Environ Pollut* 231:954–970. <https://doi.org/10.1016/j.envpol.2017.08.032>
9. Unuabonah EI, Nöske R, Weber J et al (2019) New micro/mesoporous nanocomposite material from low-cost sources for the efficient removal of aromatic and pathogenic pollutants from water. *Beilstein J Nanotechnol* 10:119–131. <https://doi.org/10.3762/bjnano.10.11>
10. Elliott M (2003) Biological pollutants and biological pollution—an increasing cause for concern. *Mar Pollut Bull* 46:275–280. [https://doi.org/10.1016/S0025-326X\(02\)00423-X](https://doi.org/10.1016/S0025-326X(02)00423-X)
11. Hachani C, Lamhamedi MS, Cameselle C et al (2020) Effects of wctomycorrhizal fungi and heavy metals (Pb, Zn, and Cd) on growth and mineral nutrition of *Pinus halepensis* seedlings in North Africa. *Microorg* 8
12. Kaya N, Yıldız Uzun Z, Altuncan C, Uzun H (2022) Adsorption of Congo red from aqueous solution onto KOH-activated biochar produced via pyrolysis of pine cone and modeling of the process using artificial neural network. *Biomass Convers Biorefinery* 12:5293–5315. <https://doi.org/10.1007/s13399-021-01856-5>
13. Akhter F, Zoppas FM, Soomro M et al (2021) Carbon-based sorbents for heavy metal removal from aqueous solution, discrepancies, and future prospects: a state-of-the-art review. *Biomass Convers Biorefinery*. <https://doi.org/10.1007/s13399-021-01866-3>
14. Saravanan A, Kumar PS, Yaashikaa PR et al (2021) Mixed biosorbent of agro waste and bacterial biomass for the separation of Pb(II) ions from water system. *Chemosphere* 277:130236. <https://doi.org/10.1016/j.chemosphere.2021.130236>
15. Ahmad MA, Ahmed NA, Adesina Adegoke K, Bello OS (2020) Trapping synthetic dye molecules using modified lemon grass adsorbent. *J Dispers Sci Technol* 43:583–597. <https://doi.org/10.1080/01932691.2020.1844016>
16. Bello OS, Alabi EO, Adegoke KA et al (2020) Rhodamine B dye sequestration using *Gmelina aborea* leaf powder. *Heliyon* 6:e02872. <https://doi.org/10.1016/j.heliyon.2019.e02872>
17. Nouacer I, Benalia M, Henini G et al (2021) Mathematical modeling and interpretation of equilibrium isotherms of Pb (II) from aqueous media by *Chlorella pyrenoidosa* immobilized in *Luffa cylindrica*. *Biomass Convers Biorefinery*. <https://doi.org/10.1007/s13399-021-01722-4>
18. Dineshkumar R, Sowndariya M, Kalaiselvi S et al (2022) Effective removal of lead (Pb) by natural biosorbent marine microalgae (*Dunaliella salina*) through batch experiment. *Biomass Convers Biorefinery*. <https://doi.org/10.1007/s13399-021-02260-9>
19. Kazak O, Tor A (2020) In situ preparation of magnetic hydrochar by co-hydrothermal treatment of waste vinasse with red mud and its adsorption property for Pb(II) in aqueous solution. *J Hazard Mater* 393:122391. <https://doi.org/10.1016/j.jhazmat.2020.122391>
20. Foroutan R, Mohammadi R, Farjadfard S et al (2019) Characteristics and performance of Cd, Ni, and Pb bio-adsorption using *Callinectes sapidus* biomass: real wastewater treatment. *Environ Sci Pollut Res* 26:6336–6347. <https://doi.org/10.1007/s11356-018-04108-8>
21. Sarat Chandra T, Mudliar SN, Vidyashankar S et al (2015) Defatted algal biomass as a non-conventional low-cost adsorbent:

- surface characterization and methylene blue adsorption characteristics. *Bioresour Technol* 184:395–404. <https://doi.org/10.1016/j.biortech.2014.10.018>
22. Iqbal M, Saeed A, Zafar SI (2009) FTIR spectrophotometry, kinetics and adsorption isotherms modeling, ion exchange, and EDX analysis for understanding the mechanism of Cd<sup>2+</sup> and Pb<sup>2+</sup> removal by mango peel waste. *J Hazard Mater* 164:161–171. <https://doi.org/10.1016/j.jhazmat.2008.07.141>
  23. Feng N, Guo X, Liang S et al (2011) Biosorption of heavy metals from aqueous solutions by chemically modified orange peel. *J Hazard Mater* 185:49–54. <https://doi.org/10.1016/j.jhazmat.2010.08.114>
  24. Memon JR, Memon SQ, Bhangar MI et al (2009) Banana peel: a green and economical sorbent for the selective removal of Cr(VI) from industrial wastewater. *Colloids Surf B Biointerfaces* 70:232–237. <https://doi.org/10.1016/j.colsurfb.2008.12.032>
  25. Razmi FA, Ngadi N, Wong S et al (2019) Kinetics, thermodynamics, isotherm and regeneration analysis of chitosan modified pandan adsorbent. *J Clean Prod* 231:98–109. <https://doi.org/10.1016/j.jclepro.2019.05.228>
  26. Mamba G, Mishra AK (2016) Graphitic carbon nitride (g-C<sub>3</sub>N<sub>4</sub>) nanocomposites: a new and exciting generation of visible light driven photocatalysts for environmental pollution remediation. *Appl Catal B Environ* 198:347–377. <https://doi.org/10.1016/j.apcatb.2016.05.052>
  27. Unuabonah EI, Kolawole MO, Agunbiade FO et al (2017) Novel metal-doped bacteriostatic hybrid clay composites for point-of-use disinfection of water. *J Environ Chem Eng* 5:2128–2141. <https://doi.org/10.1016/j.jece.2017.04.017>
  28. Anantha RK, Kota S (2016) An evaluation of the major factors influencing the removal of copper ions using the egg shell (*Dromaius novaehollandiae*): chitosan (*Agaricus bisporus*) composite. *3 Biotech* 6:1–16. <https://doi.org/10.1007/s13205-016-0381-2>
  29. Chowdhury S, Das SP (2013) Artificial neural network (ANN) modeling of adsorption of methylene blue by NaOH-modified rice husk in a fixed-bed column system. *Environ Sci Pollut Res* 20:1050–1058. <https://doi.org/10.1007/s11356-012-0912-2>
  30. Ho Y-S, Ofomaja AE (2006) Pseudo-second-order model for lead ion sorption from aqueous solutions onto palm kernel fiber. *J Hazard Mater* 129:137–142. <https://doi.org/10.1016/j.jhazmat.2005.08.020>
  31. Omorogie MO, Ilesanmi FO, Alfred MO, Helmreich B (2022) Thermally-treated MgO/nanocrystalline cellulose immobilized onto a Santa Barbara-16 mesoporous SiO<sub>2</sub> template for the sequestration of antibiotics from polluted water. *New J Chem* 46:20918–20931. <https://doi.org/10.1039/D2NJ03611H>
  32. Langfield RD, Scarano FJ, Heitzman ME et al (2004) Use of a modified microplate bioassay method to investigate antibacterial activity in the Peruvian medicinal plant *Peperomia galioides*. *J Ethnopharmacol* 94:279–281. <https://doi.org/10.1016/j.jep.2004.06.013>
  33. Aida P, Rosa V, Blamea F, Thomas A, Salvador C (2001) Parauan plants used in traditional medicine. *Short Commun J Ethnopharmacol* 16:93–98
  34. Adeleke O, Akinlabi S, Jen T-C, Dunmade I (2022) A machine learning approach for investigating the impact of seasonal variation on physical composition of municipal solid waste. *J Reliab Intell Environ*. <https://doi.org/10.1007/s40860-021-00168-9>
  35. Güldal V, Tongal H (2010) Comparison of recurrent neural network, adaptive neuro-fuzzy inference system and stochastic models in Eğirdir Lake level forecasting. *Water Resour Manag* 24:105–128. <https://doi.org/10.1007/s11269-009-9439-9>
  36. Mustapha M, Mustafa MW, Khalid SN et al (2016) Correlation and wavelet-based short-term load forecasting using anfis. *Indian J Sci Technol* 9. <https://doi.org/10.17485/ijst/2016/v9i46/107141>
  37. Adeleke O, Akinlabi S, Jen TC et al (2022) Evolutionary-based neuro-fuzzy modelling of combustion enthalpy of municipal solid waste. *Neural Comput Appl* 2. <https://doi.org/10.1007/s00521-021-06870-2>
  38. Tang Y, Yin M, Yang W et al (2019) Emerging pollutants in water environment: occurrence, monitoring, fate, and risk assessment. *Water Environ Res a Res Publ Water Environ Fed* 91:984–991. <https://doi.org/10.1002/wer.1163>
  39. Ghosh S, Hazarika AP, Chandra A, Mudi RK (2021) Adaptive neighbor constrained deviation sparse variant fuzzy c-means clustering for brain MRI of AD subject. *Vis Informatics* 5:67–80. <https://doi.org/10.1016/j.visinf.2021.12.001>
  40. Gao Y, Wang Z, Xie J, Pan J (2022) A new robust fuzzy c-means clustering method based on adaptive elastic distance. *Knowledge-Based Syst* 237:107769. <https://doi.org/10.1016/j.knsys.2021.107769>
  41. Wei M, Bai B, Sung AH et al (2007) Predicting injection profiles using ANFIS. *Inf Sci (Ny)* 177:4445–4461. <https://doi.org/10.1016/j.ins.2007.03.021>
  42. Abonyi J, Andersen H, Nagy L, Szeifert F (1999) Inverse fuzzy-process-model based direct adaptive control. *Math Comput Simul* 51:119–132. [https://doi.org/10.1016/s0378-4754\(99\)00142-1](https://doi.org/10.1016/s0378-4754(99)00142-1)
  43. Kyei SK, Akaranta O, Darko G (2020) Synthesis, characterization and antimicrobial activity of peanut skin extract-azo-compounds. *Sci African* 8:e00406. <https://doi.org/10.1016/j.sciaf.2020.e00406>
  44. Kohan Baghkeirati E, Bagherieh-Najjar MB, Khandan Fadafan H, Abdolzadeh A (2016) Synthesis and antibacterial activity of stable bio-conjugated nanoparticles mediated by walnut (*Juglans regia*) green husk extract. *J Exp Nanosci* 11:512–517. <https://doi.org/10.1080/17458080.2015.1090020>
  45. Mandal C, Sahu M (2021) Application of metal and metal oxide nanoparticles as potential antibacterial agents BT. In: Singh SP, Rathinam K, Gupta T, Agarwal AK (eds) *Nanomaterials and nanocomposites for environmental remediation*. Springer Singapore, pp 121–140
  46. Unuabonah EI, Ugwuja CG, Omorogie MO et al (2018) Clays for efficient disinfection of bacteria in water. *Appl Clay Sci* 151:211–223. <https://doi.org/10.1016/j.clay.2017.10.005>
  47. Lam SS, Liew RK, Wong YM et al (2017) Microwave-assisted pyrolysis with chemical activation, an innovative method to convert orange peel into activated carbon with improved properties as dye adsorbent. *J Clean Prod* 162:1376–1387. <https://doi.org/10.1016/j.jclepro.2017.06.131>
  48. Garba ZN, Rahim AA, Bello BZ (2015) Optimization of preparation conditions for activated carbon from *Brachystegia eurycoma* seed hulls: a new precursor using central composite design. *J Environ Chem Eng* 3:2892–2899. <https://doi.org/10.1016/j.jece.2015.10.017>
  49. Marsagishvili T, Tatishvili G, Ananiashvili N et al (2020) Adsorption of lead ions on carbonaceous sorbents of nutshell obtained from secondary raw material BT. In: Tiginyanu I, Sontea V, Railean S (eds) *4th International Conference on Nanotechnologies and Biomedical Engineering*. Springer International Publishing, Cham, pp 97–100
  50. Pandey S, Fosso-Kankeu E, Spiro MJ et al (2020) Equilibrium, kinetic, and thermodynamic studies of lead ion adsorption from mine wastewater onto MoS<sub>2</sub>-clinoptilolite composite. *Mater Today Chem* 18:100376. <https://doi.org/10.1016/j.mtchem.2020.100376>
  51. Alghamdi AA, Al-Odayni AB, Saeed WS et al (2019) Efficient adsorption of lead (II) from aqueous phase solutions using

- polypyrrole-based activated carbon. *Materials* (Basel) 12. <https://doi.org/10.3390/ma12122020>
52. Sabela MI, Kunene K, Kanchi S et al (2019) Removal of copper (II) from wastewater using green vegetable waste derived activated carbon: an approach to equilibrium and kinetic study. *Arab J Chem* 12:4331–4339. <https://doi.org/10.1016/j.arabjc.2016.06.001>
53. Yu F, Li Y, Han S, Ma J (2016) Adsorptive removal of antibiotics from aqueous solution using carbon materials. *Chemosphere* 153:365–385. <https://doi.org/10.1016/j.chemosphere.2016.03.083>
54. Samuel MS, Shah SS, Bhattacharya J et al (2018) Adsorption of Pb(II) from aqueous solution using a magnetic chitosan/graphene oxide composite and its toxicity studies. *Int J Biol Macromol* 115:1142–1150. <https://doi.org/10.1016/j.ijbiomac.2018.04.185>
55. Narasimharao K, Lingamdinne LP, Al-Thabaiti S et al (2022) Synthesis and characterization of hexagonal MgFe layered double hydroxide/graphene oxide nanocomposite for efficient adsorptive removal of cadmium ion from aqueous solutions: Isotherm, kinetic, thermodynamic and mechanism. *J Water Process Eng* 47:102746. <https://doi.org/10.1016/j.jwpe.2022.102746>
56. Adegoke KA, Adeleke O, Adesina MO et al (2022) Clean technology for sequestering Rhodamine B dye on modified mango pod using artificial intelligence techniques. *Curr Res Green Sustain Chem* 5. <https://doi.org/10.1016/j.crgsc.2022.100275>
57. Zhou K, Yang S (2020) Effect of cluster size distribution on clustering: a comparative study of k-means and fuzzy c-means clustering. *Pattern Anal Appl* 23:455–466. <https://doi.org/10.1007/s10044-019-00783-6>
58. Adeleke O, Akinlabi SA, Jen T-C, Dunmade I (2020) Prediction of municipal solid waste generation: an investigation of the effect of clustering techniques and parameters on ANFIS model performance. *Environ Technol* 43:1634–1647
59. Tao HC, Zhang HR, Li JB, Ding WY (2015) Biomass based activated carbon obtained from sludge and sugarcane bagasse for removing lead ion from wastewater. *Bioresour Technol* 192:611–617. <https://doi.org/10.1016/j.biortech.2015.06.006>
60. Ramola S, Belwal T, Li CJ et al (2020) Improved lead removal from aqueous solution using novel porous bentonite - and calcite-biochar composite. *Sci Total Environ* 709:136171. <https://doi.org/10.1016/j.scitotenv.2019.136171>
61. Tashauoei HR, Hashemi S, Ardani R et al (2016) Adsorption of lead from aqueous solution by modified beech sawdust. *J Saf Environ Health Res* 1:11–16. <https://doi.org/10.22053/jsehr.2016.33382>
62. Basu M, Guha AK, Ray L (2017) Adsorption of lead on cucumber peel. *J Clean Prod* 151:603–615. <https://doi.org/10.1016/j.jclepro.2017.03.028>
63. Forghani M, Azizi A, Livani MJ, Kafshgari LA (2020) Adsorption of lead(II) and chromium(VI) from aqueous environment onto metal-organic framework MIL-100(Fe): synthesis, kinetics, equilibrium and thermodynamics. *J Solid State Chem* 291:121636. <https://doi.org/10.1016/j.jssc.2020.121636>
64. Ghogomu MSN, Ajifack DL et al (2016) Adsorption of lead (II) from aqueous solution using activated carbon prepared from raffia palm (*Raphia hookeri*) fruit epicarp. *IOSR J Appl Chem* 9:74–85. <https://doi.org/10.9790/5736-0907017485>

**Publisher's Note** Springer Nature remains neutral with regard to jurisdictional claims in published maps and institutional affiliations.